Journal of Catalysis 285 (2012) 273–284

Contents lists available at SciVerse ScienceDirect

Journal of Catalysis

journal homepage: www.elsevier.com/locate/jcat

An integrated approach to Deacon chemistry on RuO_2-based catalysts

Detre Teschner [a,d,*], Ramzi Farra [a], Lide Yao [a,1], Robert Schlögl [a], Hary Soerijanto [b], Reinhard Schomäcker [b], Timm Schmidt [c], László Szentmiklósi [d], Amol P. Amrute [e], Cecilia Mondelli [e], Javier Pérez-Ramírez [e], Gerard Novell-Leruth [f], Núria López [f,*]

[a] Fritz-Haber Institute of the Max Planck Society, Berlin D-14195, Germany
[b] Department of Chemistry, Technical University of Berlin, Berlin D-10623, Germany
[c] Bayer MaterialScience AG, PUR-PTI-PRI New Processes Isocyanates, Dormagen D-41538, Germany
[d] Institute of Isotopes, Hungarian Academy of Sciences, Budapest H-1525, Hungary
[e] Institute for Chemical and Bioengineering, Department of Chemistry and Applied Biosciences, ETH Zurich, HCI E 125, Wolfgang-Pauli-Strasse 10, CH-8093 Zurich, Switzerland
[f] Institute of Chemical Research of Catalonia (ICIQ), Av. Paisos Catalans 16, Tarragona 43007, Spain

ARTICLE INFO

Article history:
Received 9 May 2011
Revised 3 August 2011
Accepted 29 September 2011
Available online 8 November 2011

Keywords:
HCl oxidation
RuO_2/SnO_2
HRTEM
PGAA
TAP
DFT
Kinetics
Deacon reaction

ABSTRACT

Rationally designed RuO_2-based Deacon catalysts can contribute to massive energy saving compared to the current electrolysis process in chemically recycling HCl to produce molecular chlorine. Here, we report on our integrated approach between state-of-the-art experiments and calculations. The aim is to understand industrial Deacon catalyst in its realistic surface state and to derive mechanistic insights into this sustainable reaction. We show that the practically relevant RuO_2/SnO_2 consists of two major RuO_2 morphologies, namely 2–4 nm-sized particles and 1–3-ML-thick epitaxial RuO_2 films attached to the SnO_2 support particles. A large fraction of the small nanoparticles expose {1 1 0} and {1 0 1} facets, whereas the film grows with the same orientations, due to the preferential surface orientation of the rutile-type support. Steady-state Deacon kinetics indicate a medium-to-strong positive effect of the partial pressures of reactants and deep inhibition by both water and chlorine products. Temporal Analysis of Products and in situ Prompt Gamma Activation Analysis strongly suggest a Langmuir–Hinshelwood mechanism and that adsorbed Cl poisons the surface. Under relevant operation conditions, the reactivity is proportional to the coverage of a specific atomic oxygen species. On the extensively chlorinated surface that can be described as surface oxy-chloride, oxygen activation is the rate-determining step. DFT-based micro-kinetic modeling reproduced all experimental observations and additionally suggested that the reaction is structure sensitive. Out of the investigated models, the 2 ML RuO_2 film-covered SnO_2 gives rise to significantly higher reactivity than the (1 0 1) surface, whereas the 1 ML film seems to be inactive.

1. Introduction

Chlorine is used as reactive intermediate in many processes to create thousands of often indispensable products of the chemical industry. The annual production of Cl_2 is ca. 50 Mton and has an expected demand growth of 4.4% per year in the period 2010–2015 [1]. Upon use, large amounts of Cl_2 are reduced to HCl or chloride salts. The most prominent example is the phosgene-mediated isocyanate production (e.g., 4 mol HCl per mol of toluene diisocyanate). By-product HCl, pure or absorbed in water to produce hydrochloric acid, is typically used in other processes, e.g., as acid catalyst, for the neutralization of alkaline streams, as chlorine source in PVC production, or is recycled by electrolysis to chlorine; this latter is, however, a highly energy-demanding process. The catalytic oxidation of by-product HCl to Cl_2, the Deacon process ($2HCl + 1/2O_2 \rightarrow Cl_2 + H_2O$), is an energetically efficient yet environmentally friendly solution to create a complete recycle process. However, the long-term implementation of all processes developed since the original Deacon concept has failed namely due to the short catalyst lifetime [2–4]. Only recently, Sumitomo and Bayer have succeeded in turning HCl oxidation into industrial reality with the use of RuO_2-based catalysts [5–12]. As Sumitomo has shown, the choice of the support is particularly crucial [8]. The "trick" to stabilize the catalyst is, in fact, to apply a support stabilizing epitaxially the active phase. In the 1960s, Shell had already introduced a silica-supported Ru-based system in the HCl oxidation process, but a much less active and stable catalyst was obtained [13]. Despite a number of studies addressing the

* Corresponding authors. Address: Fritz-Haber Institute of the Max Planck Society, Faradayweg 4-6, Berlin D-14195, Germany. Fax: +49 30 84134676 (D. Teschner), fax: +34 97792231 (N. López).
E-mail addresses: teschner@fhi-berlin.mpg.de (D. Teschner), nlopez@iciq.es (N. López).
[1] Present address: Department of Applied Physics, Aalto University School of Science and Technology, Aalto, Finland.

0021-9517 © 2011 Elsevier Inc. Open access under CC BY-NC-ND license.
doi:10.1016/j.jcat.2011.09.039

mechanism of HCl oxidation on RuO_2 single crystals [14–17], little is known about structure and function of the polycrystalline supported catalysts [18]. Furthermore, the approaches have generally been based on limited experimental or computational methods.

We present here an integrated approach to unravel HCl oxidation on the industrially relevant RuO_2/SnO_2 catalyst. Synthesis and basic characterization have been combined with steady-state tests in a dedicated plug-flow reactor. In situ studies using Prompt Gamma Activation Analysis (PGAA), Temporal Analysis of Products (TAP), and Density Functional Theory (DFT) simulations coupled to micro-kinetic (MK) analysis were used to obtain complementary insights into the structure and function of this current Bayer system. This improved and deeper knowledge may enable designing new and cheaper materials capable to act as catalysts in this demanding reaction.

2. Experimental section

2.1. Catalyst preparation

RuO_2/SnO_2 was prepared by dry impregnation. Commercially available SnO_2-cassiterite (Keeling & Walker, Superlite C) was calcined for 2 h at 1273 K prior to use in order to ensure the formation of the rutile-type structure also at a surface level. Impregnation was performed with a $RuCl_3$ aqueous solution (nominal 2 wt% Ru). The obtained material was dried at 333 K for 5 h and calcined at 523 K under air for 16 h. Low-temperature calcination was used to prevent extensive agglomeration of the Ru-phase, thus achieving a higher dispersion. A parallel preparation was carried out using additional alumina binder (γ-Al_2O_3, 200 $m^2\,g^{-1}$; Saint-Gobain NorPro) prior to impregnation to further stabilize the catalytic performance and hence reach industrially relevant long-term (over a year) stability. The longevity of this catalyst was very recently demonstrated in mini-plant tests using 2 mm spherical bodies [19]. The two catalysts display similar performance (e.g., comparable O_2 dependence in in situ PGAA and kinetic experiment), except for the long-term stability. Hence, to enable structure–function correlations, characterization was performed on the binder-free (RuO_2/SnO_2) sample. However, kinetic experiments (transient and steady-state), for which stability is of utmost importance, will be discussed using the data for the binder-stabilized (RuO_2/SnO_2–Al_2O_3) catalyst. Bulk RuO_2 (Aldrich, 99.9%) was employed as reference material in transient kinetic studies. Prior to use, the as-received oxide powder was calcined in static air at 773 K (10 K min^{-1}) for 5 h.

2.2. Catalytic tests

For steady-state kinetic measurements, the binder-containing catalyst was first powdered by ball milling and diluted with a five-fold amount of SnO_2 support material. Water was added to the powder mixture and then it was dried at 353 K. A sieve fraction of 0.2–0.45 mm-sized particles was prepared, and 1 g of it was diluted with 4 g glass beads and mixed well in order to minimize the occurrence of hot spots in the reactor. An atmospheric pressure reactor operated at 573 K was fed with a range of reactant gas mixtures by using mass flow controllers, and Cl_2 formation was detected by iodometric titration. The catalytic tube reactor was made of quartz with 8 mm inner diameter. Various reaction feed compositions with a total flow of 80 $cm^3\,min^{-1}$ were used to evaluate the formal kinetic dependence of the reaction rate to the reactants and products. The partial pressures of the reactants were varied in the range of 0.0625–0.5 bar, and water was set between 0–0.5 bar, whereas Cl_2 was co-fed up to 0.2 bar. Conversion level was below 10% to allow kinetic evaluation. By calculating the Knudsen diffusion coefficient and the Wheeler–Weisz modulus, it was verified that the reaction was not limited by intraparticle diffusion.

2.3. Catalyst characterization

Standard characterization of RuO_2/SnO_2 was carried out by N_2 adsorption at 77 K, inductively coupled plasma mass spectrometry (ICP-MS), X-ray diffraction (XRD), and temperature-programmed reduction with hydrogen (H_2-TPR). Micro-structural and chemical characterizations (elemental mapping) of the binder-free catalyst were performed on a Titan 80–300 kV aberration-corrected Transmission Electron Microscope (TEM). For experimental details to these methods, see the Supplementary information.

2.4. In situ Prompt Gamma Activation Analysis

In situ Prompt Gamma Activation Analysis (PGAA) is a technique recently implemented for studying catalysts in action [20]. It is based on the radiative neutron capture of nuclei, that is, with using cold neutrons excitation element specific gamma rays are emitted, enabling the quantification of elements in the investigated volume, in our case inside a Deacon micro-reactor. The aim of our experiments was to quantify in situ the Cl uptake of Deacon catalysts under various steady-state reaction conditions and correlate this information with the catalytic performance. PGAA at atmospheric pressure condition was carried out at the cold neutron beam of the Budapest Neutron Centre [21]. A Compton-suppressed high-purity germanium crystal was used to detect the prompt gamma photons. Molar ratios (Cl/Ru) were determined from the characteristic peak areas corrected by the detector efficiency and the nuclear data of the observed elements [22]. For the experiments, the same quartz tube reactor as for the steady-state kinetic study was placed into the neutron beam and the reactor tube was surrounded by a specially designed oven having openings for the incoming and outgoing neutrons and for the emitted gamma rays. These openings are covered by thin aluminum foils for decreasing heat losses. 0.9 g of RuO_2/SnO_2 of sieve fraction 0.1–0.2 mm was loaded into the reactor. An experimental series with RuO_2/SnO_2–Al_2O_3 was also carried out with similar results as will be detailed here later. These latter data are included in Supplementary information. Reaction feed, at constant 166.6 $cm^3\,min^{-1}$ total flow, was supplied by mass flow controllers, and the feed composition was varied between O_2:HCl:N_2 = 0.25:1:3.75 and 4:1:0. The reaction was monitored by iodometric titration. The reaction temperature was set to 573 K for the p(O_2)-dependent experiment, which was performed after a HCl treatment at the same temperature to saturate the catalyst surface with chlorine. In a separate experiment at 523 K, the Cl uptake was acquired with time on stream.

2.5. Temporal Analysis of Products

Transient mechanistic studies of HCl oxidation over RuO_2/SnO_2, RuO_2/SnO_2–Al_2O_3, and RuO_2 were carried out in the TAP-2 reactor [23,24]. This technique has been successfully applied to derive mechanistic fingerprints of the Deacon reaction over metal oxides [18,25,26]. RuO_2/SnO_2–Al_2O_3 and RuO_2 were investigated in fresh form, while RuO_2/SnO_2 was equilibrated for 50 h under Deacon conditions (HCl:O_2:He = 2:4:4, 1 bar, 623 K, W/F^0 = 4.5 g h mol_{HCl}^{-1}) prior to the TAP study. The equilibration protocol has been detailed elsewhere [19]. The samples (10 mg, particle size = 0.2–0.3 mm) were loaded in the isothermal (central) zone of a quartz micro-reactor (4.6 mm i.d., 71 mm long), between two layers of quartz particles of the same particle size. The samples were pretreated in O_2 (20 cm^3 STP min^{-1}) at 623 K and ambient pressure for 1 h. Thereafter, they were evacuated to 10^{-10} bar and TAP experiments were

carried out at 623 K using a pulse size of ca. 10^{16} molecules. This large pulse size, exceeding the Knudsen diffusion regime, was required in order to properly detect reaction products, mainly Cl_2, by mass spectrometry. Since current TAP theories for modeling purposes are limited to operation in the Knudsen regime (pulses), quantitative micro-kinetic analysis was not attempted from the present TAP results. Pulses of a HCl–O_2 mixture (HCl:O_2:Kr = 2:1:1) were followed by pump–probe experiments of O_2:Ar = 2:1 and HCl:Kr = 5:1 from two separate high-speed valves. In the latter measurements, the O_2 pulse is separated from the HCl pulse by a time delay (Δt) of 1–12 s; 10 s after pulsing the probe molecule, a new cycle starts by pulsing the pump molecule and so on. In the TAP experiments, Kr (Linde, purity 5.0), Ar (Linde, purity 5.0), O_2 (Air Products, purity 5.2), and HCl (Praxair, purity 2.5) were used. A quadrupole mass spectrometer (RGA 300, Stanford Research Systems) was used for monitoring the transient responses at the reactor outlet of the following atomic mass units (AMUs): 84 (Kr), 70 (Cl_2), 40 (Ar), 36 (HCl), 32 (O_2), and 18 (H_2O). The transient responses displayed in this article correspond to an average of 10 pulses per AMU in order to improve the signal-to-noise ratio. Prior to that, it was checked that the responses were stable, that is, with invariable intensity and shape during an interval of at least 20 pulses.

2.6. First principles simulations and micro-kinetic modeling

Density Functional Theory (DFT) applied to slabs representing the lowest-index facets of RuO_2 was employed to determine the thermodynamic and kinetic parameters for HCl oxidation. The VASP code was employed in the calculations [27,28]. The exchange–correlation functional was RPBE [29], and the inner electrons were replaced by PAW pseudopotentials [30] while monoelectronic valence states were expanded in plane waves with a cutoff energy of 400 eV. For RuO_2, we employed the (110), (101), and (100) surfaces (Fig. 1), each of the slabs contains three trilayers of Ru_2O_4 stoichiometry. On these surfaces ((110), (101) and (100)), two kinds of surface oxygen atoms can be identified. First of all, threefold-coordinated O_{3c} positions are present. This is the same coordination as for the oxygen atoms in the bulk. Some O atoms only show a coordination of two and are usually denoted as bridge oxygen atoms, O_b. Ru cations are also present at the surface with a coordination number of five. This is lower than that in the bulk (6) and, thus, these Ru atoms are denoted as under-coordinated, Ru_{cus} sites. These O_b, O_{3c}, and Ru_{cus} motives are common to all low-index facets and are thus expected to be present even for less well-defined surfaces. To describe the different positions at the surfaces, we employ the subindexes "b," if a given atom or fragment is adsorbed at a formerly O_b position, and "cus," if adsorbed at a formerly open Ru_{cus} site. To represent the RuO_2/SnO_2 catalyst, on top of SnO_2(110), either one (model RuO_2/SnO_2(1 ML)) or two (model RuO_2/SnO_2(2 ML)) epilayers of RuO_2 were accommodated (Fig. S.I. 1). The total thickness of these slabs corresponds to five layers where the upper three layers were relaxed in all directions.

With the surface energies of the low-index facets, the structure of equilibrium nanoparticles can be calculated through the Wulff construction [31]. Calculations on pure RuO_2 have shown a good agreement with XRD estimates [16]. The Wulff structure provides about a 43% of RuO_2(110), 42% of RuO_2(101), and approximately 15% of RuO_2(100). Other facets as RuO_2(001) show a high surface energy, and thus, in this study, we consider only those mentioned above. In order to analyze the complete Deacon process on RuO_2 nanoparticles, we have considered the individual reaction paths on the most representative structures ((110) and (101)) indicated above. Then, the rate was obtained through micro-kinetic simulations, MK. A detailed description of the procedure is presented in Supplementary information and can be summarized as follows: the rate is calculated as the sum of the individual rates of the different facets weighted by their contribution to the nanoparticle obtained from the Wulff construction based on the DFT values. In order to do this, the rate coefficients for the elementary steps were evaluated using the thermodynamic, kinetic, and partition functions obtained from the DFT calculations and according to Transition State Theory [32]. The MK simulations were performed through a batch-model reactor with the setup previously employed by us for ammonia oxidation on platinum [33]. The set of differential–algebraic equations in the MK model has been resolved with Maple™ [34]. In the simulations, the initial relative pressures and temperatures correspond to those employed experimentally and also the number of particles initially contacting the surface has been balanced with respect to those in the experiments. From the MK models, several parameters have been obtained, like the apparent activation energy, the inhibition effect by reaction products, and the correlation between the species on the surface and the reaction rate. Further details to our theoretical approach, together with equilibrium constants for each of the reactions, calculated core-level shifts, and vibrational frequencies of some adsorbed species can be found in Supplementary information.

3. Results and discussion

3.1. Primary characterization

The Ru content in RuO_2/SnO_2, determined by ICP-MS, is 2.4 wt%, and the total surface area determined from N_2 adsorption is S_{BET} = 6 $m^2\,g^{-1}$. The specific surface of the SnO_2 support is low (S_{BET} = 9 $m^2\,g^{-1}$) due to its high temperature pretreatment prior to impregnation with the ruthenium salt. The XRD analysis of RuO_2/SnO_2 provides evidence of the SnO_2 crystalline phase only (Fig. S.I. 2). The presence of RuO_2 is not observed neither as phase

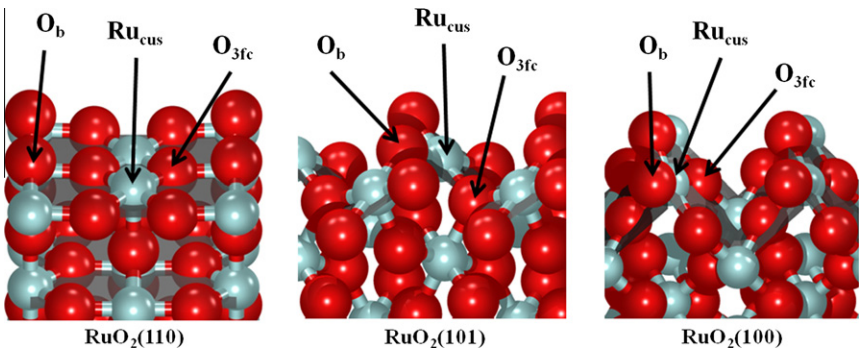

Fig. 1. Schematic representation of the RuO_2(110), (101), and (100) surfaces. Red large spheres represent O atoms, while gray ones stand for Ru. The labels for the most relevant surface centers are indicated. (For interpretation of the references to color in this figure legend, the reader is referred to the web version of this article.)

alone, owing to the relatively low ruthenium amount and the high dispersion (shown later), nor as solid solution with the support, as no peak shift of the cassiterite diffraction lines is detected. This suggests the deposition of the active phase as a thin film and/or nanoparticles covering the SnO_2 particles. The H_2-TPR profiles (Fig. S.I. 3) indicate that a higher reduction temperature is needed to reduce the supported ruthenium phase than RuO_2 alone, suggesting a strong interaction between RuO_2 and SnO_2.

3.2. Electron microscopy

The morphology of SnO_2 support particles has been revealed by TEM observations, as shown in Fig. 2a. Most particles look smooth, displaying nicely faceted feature with a mean diameter around 50 nm. Based on electron diffraction (ED) analysis (also see inset of Fig. 2a), all diffraction rings can be indexed by rutile structure, which is in agreement with the XRD data. A high-resolution TEM image in Fig. 2b clearly shows two particles with {1 1 0} and {0 1 1} facets. (We would like to remind that the families of {0 1 1} and {1 0 1} are equivalent due to the rutile symmetry.) These kinds of facets, in fact, preferentially form in rutile phase [35,36]. In contrast to the SnO_2 support particles, the RuO_2/SnO_2 catalyst particles in Fig. 2c appear rougher, suggesting the formation of ruthenium oxide nanoparticles on the support surface. Via selected area ED analysis, the RuO_2 phase was determined with the same rutile structure as the support. From EDX elemental mappings (see Fig. S.I. 4), O and Sn elements have nearly homogeneous distributions and Ru can also be detected on the support everywhere. Ru is observed especially around SnO_2 particles, as shown by the color-mixed mapping, confirming the coverage with RuO_2 layers. The high-magnification TEM image in the inset of Fig. 2c further evidences very densely packed RuO_2 particles with typical size of 2–4 nm over the SnO_2 carrier. Moreover, it can be frequently seen that some RuO_2 nanoparticles cluster into small aggregates. Besides nanoparticles, another typical morphology of thin RuO_2 film with a few atomic layers on the support is often observed, as shown in Fig. 2d. By comparing fast Fourier transformation (FFT) patterns from two selected areas, a streaking effect is remarkably visible along the [1 1 0] direction in the FFT pattern from the film area, being absent with SnO_2 only. Here, the streaking effect results from stacking faults in the thin film. Considering the same rutile structure and small lattice mismatch between RuO_2 and SnO_2, a thin film with one-two monolayer-like RuO_2 may be epitaxially formed under suitable chemical conditions, but contains a few stacking faults to some extent. Additionally, RuO_2 particles can also be epitaxially grown on SnO_2, which is, in fact, often observed in the HRTEM characterization. For instance, Fig. 2e presents a typical rutile on rutile-type micrograph, where RuO_2 particles and SnO_2 support can be easily identified by FFT analysis, with close relationships: $(1\,0\,1)RuO_2//(1\,0\,1)SnO_2$ and $(1\,1\,0)RuO_2//(1\,1\,0)SnO_2$. It is expected that there is strong interaction between RuO_2 and the SnO_2 support in these cases due to epitaxy. For the purpose of demonstrating surface orientation of RuO_2 particles, a local enlarged image close to the support's edge is shown in Fig. 2f. Clearly, RuO_2 particles expose {1 1 0} and {0 1 1} facets, in consonance with the Wulff construction in rutile. As a matter of fact, most RuO_2 particles observed expose such facets. Despite the close relation in structure, in some cases, partly due to lack of epitaxy, many other surfaces like {1 2 0} planes are exposed as well. In addition, there are various types of defects found with the RuO_2 nanoparticles, such as steps with one lattice unit, dislocations, and stacking faults.

3.3. Atmospheric catalytic tests

Since we aimed at identifying the dependence of the reaction rate on the reactants and products with high accuracy requiring thus a long-term stable material, we have selected the binder-containing RuO_2/SnO_2–Al_2O_3 catalyst for this purpose. We chose 573 K and a feed of 20 $cm^3\,min^{-1}$ O_2, 20 $cm^3\,min^{-1}$ HCl, and 40 $cm^3\,min^{-1}$ N_2 as a reference point (r_0), and normalized the reaction rate at every investigated reaction condition (r) by r_0, as shown in Fig. 3a. Within the investigated conditions, the apparent HCl reaction order is determined from differential measurements to be 0.2, whereas that of O_2 is 0.4 (Fig. 3a). This means that both reactants show a positive, though for HCl only slight, influence on the reaction rate. On the other hand, both products (Cl_2 and H_2O) strongly inhibit the reaction, as suggested by the strongly bended curves of chlorine produced determined as function of residence time (Fig. 3d). In Fig. 3b, measurements with increasing co-feed of chlorine or H_2O are depicted, with the reaction order being near −1.0 for both, Cl_2 and H_2O. This observation implies that the rates shown in Fig. 3a were not determined under accurate differential conditions, since the measured conversion varies with feed composition, and thus, this effect leads to an underestimation of the influence of the reactant pressures on the reaction rate, expressed in too low reaction orders. To circumvent this, we repeated the HCl- and O_2-dependent series with added 0.06 bar H_2O and 0.06 bar Cl_2 at the reactor inlet (Fig. 3c). In this plot, the data are again normalized to the rate at an equimolar feed of the reactants. Results show that the HCl reaction order increases to 0.5, while that of oxygen is close to 1. Based on the stoichiometric equation, $2\,HCl + 0.5\,O_2 \leftrightarrow H_2O + Cl_2$, the rate of the reaction can be expressed with the formal kinetic rate law:

$$r = \frac{K_f p_{O2}^{1} p_{HCl}^{0.5} - \frac{k_f}{\sqrt{K} p_{O2}^{-0.5} p_{HCl}^{1.5}} p_{Cl2}^{1} p_{H2O}^{1}}{1 + K_{Cl2} p_{Cl2} + K_{H2O} p_{H2O}} \quad (1)$$

where k_f is the forward rate constant, K the equilibrium constant, and K_{Cl2} and K_{H2O} are the inhibition constants of chlorine and water, respectively. The denominator represents the usual inhibition term, whereas the numerator includes the derived rate dependences. The complex reverse rate coefficient ensures that the rate goes to zero at equilibrium pressure conditions. The apparent activation energy estimated from initial rates without co-feed of product in the temperature range of 400–671 K is 69 kJ mol^{-1}. Stronger temperature dependence is expected when products are co-feed.

3.4. Theoretical modeling

The Deacon reaction, $2HCl + 1/2O_2 \rightarrow Cl_2 + H_2O$, is calculated to be exothermic with an enthalpy of −54.3 and the Gibbs free energy is −17.3 kJ mol^{-1} at 573.15 K. The calculated values are in very good agreement with those in the databases: enthalpy −57.2 kJ mol^{-1} and corresponding Gibbs free energy −20.3 kJ mol^{-1} [37]. The mechanism of the Deacon reaction can be described with the following list of elementary steps taking place on any of the surfaces mentioned in Section 2 (i.e., $RuO_2(1\,1\,0)$, $RuO_2(1\,0\,1)$, and the overlayers on SnO_2). The mechanism, first described by us [16], has been further confirmed by other DFT studies [14,17]. Although more complex re-oxidation paths have been described for the $RuO_2(1\,1\,0)$ surface [38], the equations (6–7) in the scheme correctly reproduce the main features of surface re-oxidation.

$$HCl + O^* + ^* \leftrightarrow OH^* + Cl^* \quad (2)$$

$$OH^* + OH^* \leftrightarrow H_2O^* + O^* \quad (3)$$

$$H_2O^* \leftrightarrow H_2O + ^* \quad (4)$$

$$Cl^* + Cl^* \leftrightarrow Cl_2 + 2^* \quad (5)$$

$$O_2 + 2^* \leftrightarrow O_2^{**} \quad (6)$$

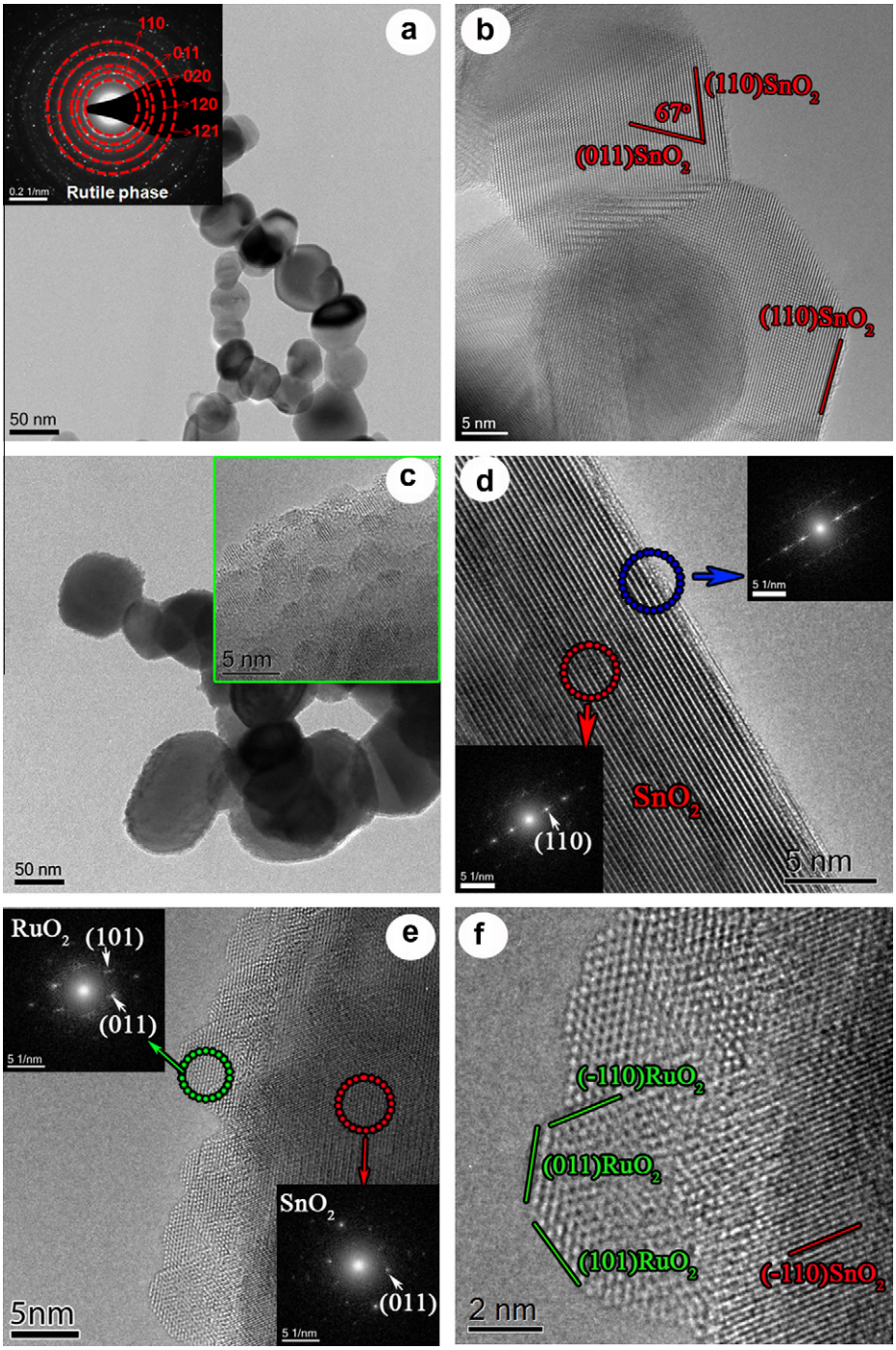

Fig. 2. (a) Overview of SnO_2-support particles by TEM and corresponding electron diffraction pattern in inset; (b) SnO_2 particles with {1 1 0} facets; (c) overview of RuO_2/SnO_2 catalyst by TEM, where inset image shows densely packed RuO_2 particles (typical size: 2–4 nm) over the SnO_2 support; (d) 1–2 monolayer-like RuO_2 film structure over the support surface; (e) RuO_2 particles are epitaxially grown on SnO_2 support (rutile on rutile); (f) HRTEM image from a local edge region in (e), where RuO_2 particles expose {1 1 0} and {0 1 1} family of facets. Note that due to the rutile symmetry (1 0 1) and (0 1 1) are equivalent facets and are thus marked as {0 1 1}.

$$O_2^{**} \leftrightarrow 2O^{*} \quad (7)$$

This list of reactions (2)–(7) indicates only the elementary steps taking place, but does not reflect the nature of the different oxygen atoms involved (either from the lattice, O_b, or from incoming O_2 molecules, O_{cus}) or the nature of the empty positions, *. Partly due to various surfaces investigated, care must be taken because the energy differences of different O species can be rather large. Moreover, even if the Deacon reaction is a redox reaction, the charges exchanged during the elementary steps are not localized in the substrate due to the metallic character of ruthenium oxide. Therefore, no charges have been associated with the intermediates in the description of the reactions (2)–(7).

In the mechanism, HCl adsorbs close to an O atom (reaction (2)) and the basic center abstracts the H atom from HCl. The source of oxygen for HCl stripping can come either from the lattice (O_b) or from newly adsorbed oxygen on the surfaces (indicated as O_{cus}). Thus, hydroxyl groups are formed on the surface, either O_bH or

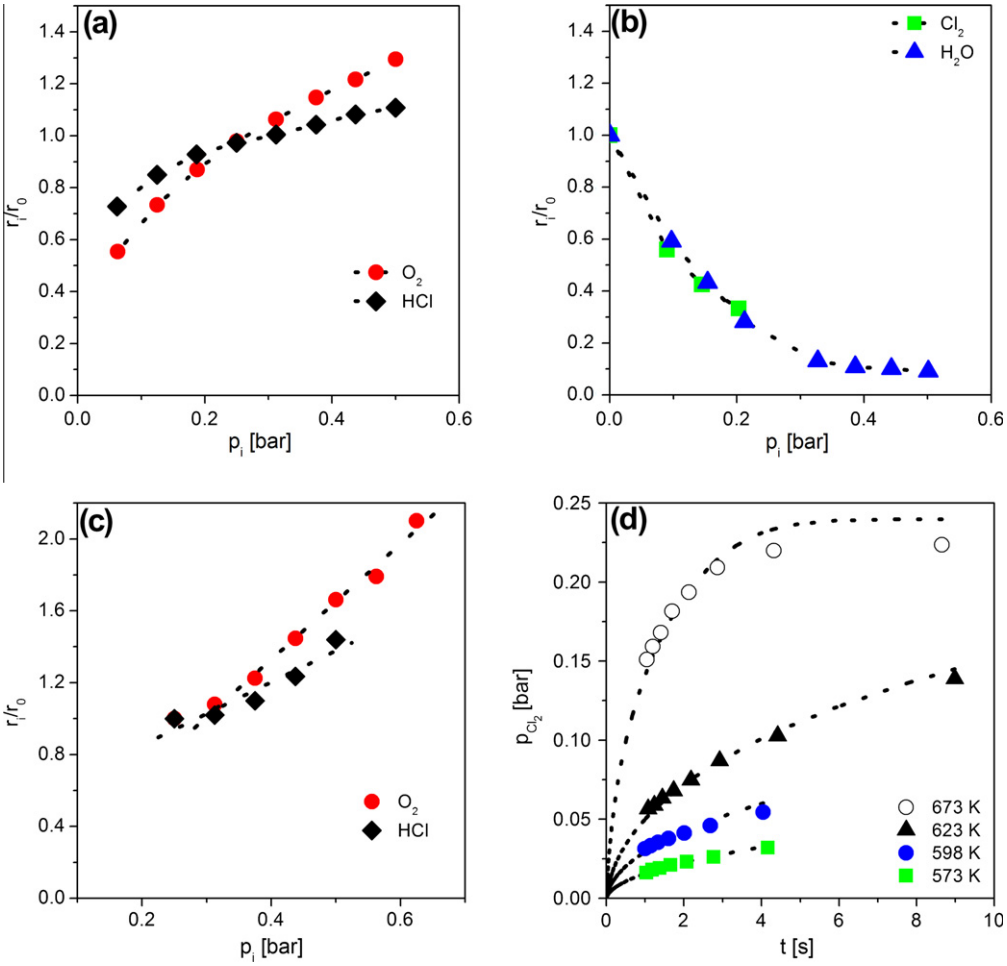

Fig. 3. The influence of (a) HCl and O_2 and (b) H_2O and Cl_2 on the reaction rate at 573 K and 1 bar in the Deacon reaction over RuO_2/SnO_2–Al_2O_3. The rate is normalized to the case 20 cm^3 min^{-1} O_2, 20 cm^3 min^{-1} HCl, and 40 cm^3 min^{-1} N_2; p_i is expressed in bar. In (c), the influence of HCl and O_2 is shown with 0.06 bar Cl_2 and 0.06 bar H_2O in the feed. Rate is normalized to the case 20 cm^3 min^{-1} O_2, 20 cm^3 min^{-1} HCl, 30 cm^3 min^{-1} N_2, 5 cm^3 min^{-1} H_2O, and 5 cm^3 min^{-1} Cl_2. In (d), the temperature is increased from 573 to 673 K in a residence time variation experiments with a feed of O_2 and HCl in a molar ratio of 1:1 without dilution with N_2. Shown is the partial pressure of Cl_2 produced.

$O_{cus}H$. These moieties can recombine on the surface to produce H_2O (reaction (3)). If water is produced at the cus centers, it can be desorbed from the surface (reaction (4)). In any case, hydroxyl recombination leaves an oxygen atom behind. This O atom can either belong to the lattice O_b or be sitting in a cus position, O_{cus}. The Cl atoms on the surface can react to form Cl_2 and desorb (reaction (5)); these taking place in one single step. The final couple of reactions correspond to surface re-oxidation and active oxygen regeneration on the surface. The dissociation of O_2 takes place from a molecularly adsorbed precursor (reaction (6)) that by interacting with two empty cus positions, finally leads to two O atoms on the surface (reaction (7)).

As indicated previously for the (1 1 0) surface, proton scavenging and hydroxyl recombination are low-energy-demanding steps. In general, we identify that bridging oxygen atoms (O_b) are effective proton scavengers. However, water desorption from bridge position is more hindered than from cus positions (0.8–1.0 eV from Ru_{cus} < 2 eV from isolated H_2O_b); therefore, O_{cus} is the preferred proton elimination species. For the (1 1 0) surface, the highest energy requirement in the mechanism corresponds to Cl recombination; however, if very high Cl coverages are present, this might not be the rate-determining step, as O_2 adsorption requires two empty neighboring Ru_{cus} sites.

To investigate the effect of surface orientation, we discuss the energy profiles for the different facets of pure RuO_2, as seen in Fig. 4a. The reaction profile for RuO_2(1 1 0) shows that the most energy-demanding step corresponds to atomic chlorine recombination. This feature is common to the other low-index facets. In addition, the RuO_2(1 0 1) energy profile shows a very similar pattern to that of the (1 1 0) facet. The largest difference is that the binding energies for all the species in the (1 1 0) are somehow larger than for the (1 0 1) surface. This affects both the surface coverage of each species and the reaction barriers that are smaller in the (1 0 1) case. Thus, a proper comparison of these surfaces requires the use of micro-kinetic analysis to evaluate the differences in activity, see the micro-kinetic modeling subsection. The (1 0 0) surface binds even less strongly intermediates, and therefore, chlorine evolution shows a much smaller energy barrier, but this is somehow compensated by the weak O_2 binding to the surface and the high barrier found for O_2 dissociation.

As already mentioned, it is possible to construct epitaxial RuO_2 layers on top of SnO_2. In this particular case, we have chosen only the (1 1 0) surfaces, as they are the most abundant. The effect of supporting RuO_2 layers on SnO_2 is reflected on the small changes induced in the electronic structure of the lattice oxygen atoms as described by the expected XPS core-level shifts (see Table S.I. 2). In the following, we concentrate on the perturbations induced on the reaction energy profiles of supported RuO_2 depicted in Fig. 4b. From the reaction profile, it is clearly shown that the single RuO_2 monolayer on SnO_2(1 1 0) binds reactants and intermediates far too strongly. For instance, the chlorine evolution barrier is close

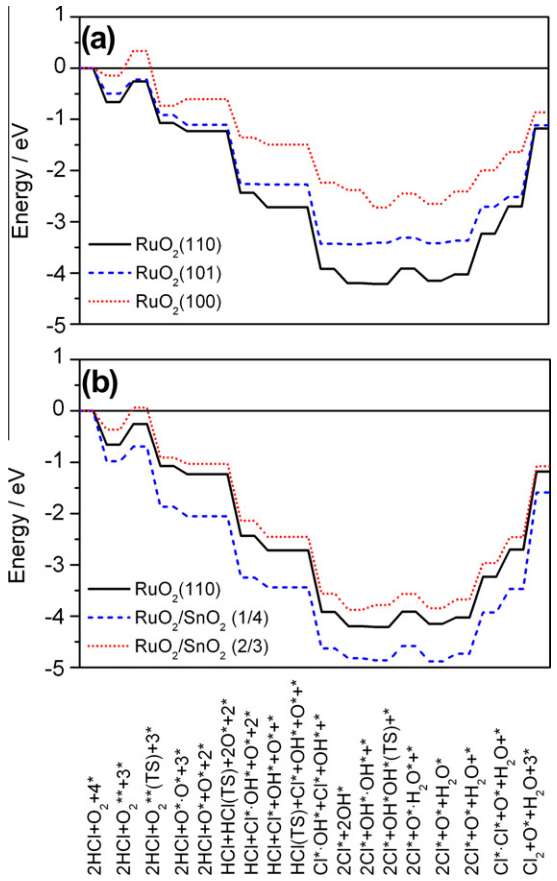

Fig. 4. Reaction energy profile for HCl oxidation on (a) pure RuO_2 lowest energy surfaces, (b) RuO_2(110) compared to one and two monolayer RuO_2 adsorbed on SnO_2(110). The profiles correspond to the reaction $2HCl + O_2 \rightarrow Cl_2 + H_2O + O^*$ leaving an oxygen atom on the surface, hence not the whole catalytic cycle is depicted. The missing steps are repetition of some of the shown ones; the complete profiles can be found in Supplementary information.

to 2 eV, in contrast to 1.54 eV found for the pure rutile case. Therefore, a single RuO_2 epitaxial monolayer is expected to be much less reactive than the pure RuO_2(110). The reasons for this behavior can be traced back to the electronic modifications induced by the presence of the SnO_2(110) support, see Figs. S.I. 7 and 8. The formation of the bimetallic overlayer implies in this particular case a higher energy of the bands associated with Ru, making them more prone to adsorption and, as a consequence, the surface is more likely to be poisoned by reaction products. The role of the electronic modifications induced by the close contact between Ru and Sn oxides is very clear for the monolayer when the density difference at the interface is computed and density accumulation at the Ru_{cus} position is favouring the interaction with electronegative adsorbates, Fig. S.I. 8. For two RuO_2 layers, the situation is, however, rather different. The binding energies of reactants and intermediates are smaller than those for the pure surface, and thus a promoting effect on the activity of the RuO_2 layers induced from the SnO_2 substrate is possible. In this case, the electronic effect described for one monolayer is already smoothed out, and instead, the geometric constraints of small lattice mismatch induced by the presence of the support (strain induced by the epitaxy to the SnO_2(110) surface) seem to control the ability of the Ru atoms to bind the reaction intermediates weaker than the pure RuO_2(110) surface. Therefore, for a single monolayer, the electronic interaction pushes the Ru levels toward the Fermi level, thus being more prone to adsorption but also to self-poisoning by Cl. As for the 2 ML case, the electronic effect is already quenched and the most important contribution comes from the strain induced by the epitaxy to the SnO_2(110) surface. This is clearly seen when comparing the Projected Density of States for 2 and 3 ML on SnO_2(110) where only small differences are observed, Fig. S.I. 7. Then, the geometric effect disturbing the Ru surroundings implies that the Ru levels are further away from the Fermi position and less active in binding reactants, intermediates, or products. Therefore, self-poisoning by Cl is less effective than for the pure RuO_2(110) surface.

A final comment regards the analysis of the chlorination of the surfaces employed in the calculations. We identified through ab initio thermodynamics that partial chlorination on the bridge positions, giving rise to the formation of surface oxy-chloride, is energetically favored [16]. Indeed, partial chlorination of the surface has been experimentally detected [18]. Nevertheless, calculations indicate that the penetration of Cl atoms inside the lattice is energetically very demanding for both RuO_2(110) and RuO_2(101), more than 2 eV. Therefore, we expect that chlorination takes place exclusively in the outermost layer by replacing some O_b or by occupying empty Ru_{cus} positions. This result will enable us to use the intrinsically bulk-sensitive PGAA as a surface-sensitive technique for this particular problem.

3.5. In situ Prompt Gamma Activation Analysis

To study chlorine uptake, and hence the Cl coverage under steady state Deacon conditions, in situ Prompt Gamma Activation Analysis was performed. Using PGAA, this can be achieved, since Cl, as mentioned above, preferentially occupies surface sites and thus, if the amount of Cl and Ru in the investigated volume is quantified and the constant gas-phase Cl contribution is subtracted, a ratio of Cl/Ru can be calculated that is proportional to the actual Cl coverage. Since we performed these measurements in different reaction mixtures, that is, with variable inlet $p(O_2)$ and fixed inlet p(HCl), we can evaluate the response of feed composition to the surface coverage, and thus, correlate the reaction rate with the surface Cl concentration. By changing the oxygen content of the feed gas, chlorine production increases with $p(O_2)$ and displays an approximately 0.4 order formal rate dependence (Fig. S.I. 5), in line with the results reported above in the kinetic analysis (without Cl_2 and H_2O co-feed) and previously reported data on RuO_2 [16]. Therefore, we can assure that our measurements do not suffer from any catalytic artifacts, and hence, the spectroscopic results can be correlated with the online catalytic data. We have also verified that RuO_2/SnO_2 slowly deactivates at the very initial stage of reaction with time on stream. This deactivation is accompanied by an increasing uptake of chlorine (Fig. 5), thus giving us a first hint that adsorbed chlorine plays a detrimental role in the reaction.

To circumvent the time-on-stream-dependent surface chlorination, in the experiments described in the following section, an initial HCl treatment was performed. In the oxygen dependent series of experiments, as stated above, increasing oxygen feed content gives rise to higher reaction rate. The measured Cl/Ru ratio does not change strongly; however a clear trend – in a relatively narrow Cl/Ru range – is observed (Fig. 6a). Higher reaction rate is reached at lower Cl/Ru ratio and, as Cl/Ru gradually increases, the reaction rate linearly decreases. This trend is characteristic of pure RuO_2 [39]; thus, we expect the contribution from the SnO_2 carrier to be negligible to the trend observed. It is worth noting that the change in the Cl/Ru ratio from 0.72 to 0.66 was the result of alteration of $HCl:O_2$ ratio in the feed from 1:0.25 to 1:4; thus, a factor of 16-fold increase in $p(O_2)$ induced a drop of Cl coverage of less than 10%. As for the binder-containing catalyst, we observe the same trend (Fig. S.I. 6); however, due to strong binding of Cl to the alumina, the Cl/Ru ratio is almost doubled. The two catalysts performed very similarly during the PGAA experiments. Due to the negative dependence of the reaction rate to the surface chlorine, one can extrapolate the chlorine content to zero activity. When

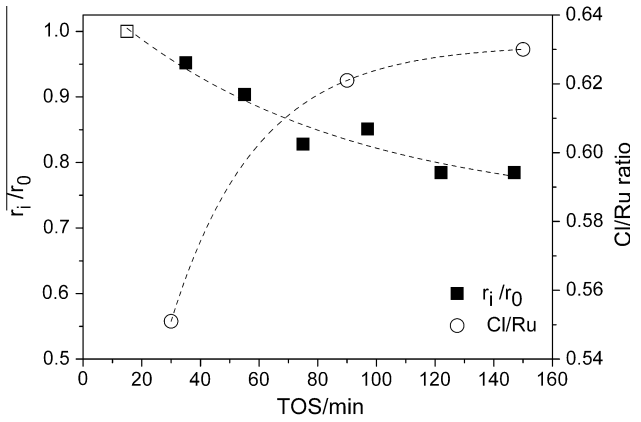

Fig. 5. Initial deactivation of RuO_2/SnO_2 at 523 K and 1 bar (feed composition: $HCl:O_2:N_2 = 1:1:3$) with the corresponding increasing Cl/Ru ratio with time-on-stream as measured by in situ PGAA. Activity is normalized to the first data point.

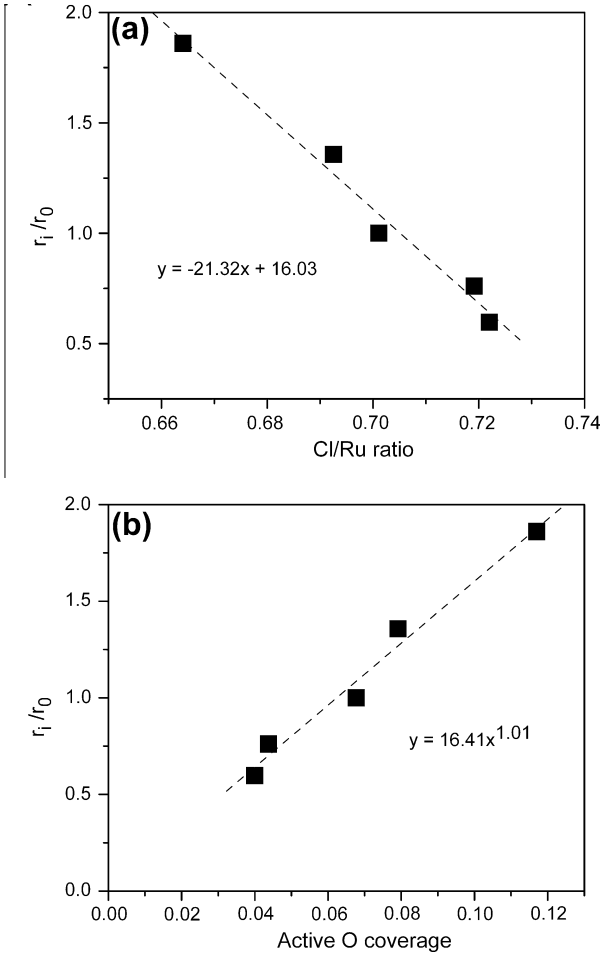

Fig. 6. Normalized reaction rate (r_i/r_0) *versus* Cl uptake (a) and of "active" O coverage (b) as measured by in situ PGAA at 573 K. Dataset corresponds to the $p(O_2)$-dependent experiment with $O_2:HCl:N_2$ varied between 0.25:1:3.75 and 4:1:0 at a total flow of 166.6 $cm^3\ min^{-1}$ and 1 bar. The r_0 reaction condition corresponds to the feed ratio 1:1:3.

normalizing the difference between the actual and the intercept chlorine content to the intercept chlorine content, one can calculate a coverage (based solely on the maximal Cl content under Deacon conditions) related to a non-Cl species that scales well with the activity. Fig. 6b shows this first-order dependence. Since adsorption of all possible species is exothermic, we expect no significant coverage of empty sites, and thus, we assign this non-Cl species to an "active" surface oxygen. Note that this is not necessarily the coverage of all possible O-based species.

3.6. Temporal Analysis of Products

The TAP technique was primarily applied (i) to qualitatively assess the influence of the SnO_2 support and the Al_2O_3 binder on the transient responses of Cl_2 and H_2O during HCl oxidation over RuO_2-based materials as well as (ii) to analyze the influence of coverage on the net Cl_2 production. Fig. 7 shows the normalized transient responses of the reaction products upon pulsing of a mixture of HCl and O_2 over fresh RuO_2/SnO_2–Al_2O_3, fresh RuO_2, and equilibrated RuO_2/SnO_2. The transients of Kr (inert gas accompanying HCl and O_2 in each pulse) are also shown for reference purposes. The shapes of the transients of Cl_2 and H_2O over the samples are comparable. This preliminarily indicates that stabilization of RuO_2/SnO_2 does not induce prominent changes in the surface properties of the ruthenium phase, as observed in parallel experiments on RuO_2/TiO_2 [18]. Still, some differences are detected. Considering the Cl_2 transients (Fig. 7a), the response of RuO_2/SnO_2–Al_2O_3 appears sharper than that of pure RuO_2. In particular, the time at maximum (t_{max}, Fig. 7d) is slightly shorter, the width at half height ($t_{h/2}$, Fig. 7d) shifted to shorter times by 0.3 s, and the tailing is less pronounced. Since the amount of chlorine produced by the supported catalyst in the TAP reactor (see non-normalized responses in Fig. 7c) is consistently higher than for RuO_2, the sharper

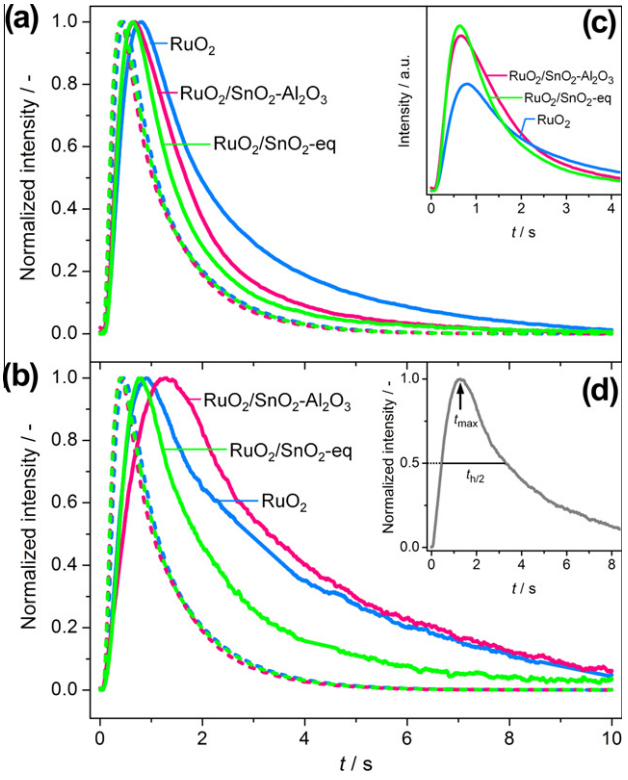

Fig. 7. Normalized transient responses of Cl_2 (a) and H_2O (b) on pulsing a mixture of $HCl:O_2 = 2:1$ at 623 K over RuO_2/SnO_2–Al_2O_3, RuO_2, and RuO_2/SnO_2-eq. The responses of the reference gas Kr are shown as dashed lines with the color of the respective catalyst material. The insets (c and d) display the non-normalized transient responses of Cl_2 over the catalysts and the graphical representation of t_{max} and $t_{h/2}$, respectively. (For interpretation of the references to color in this figure legend, the reader is referred to the web version of this article.)

Cl_2 response is related to favored chlorine evolution. This may be tentatively attributed to both the active-phase morphology and structure sensitivity of the reaction. As shown by HRTEM, the supported catalyst is constituted by a thin coat of few RuO_2 layers epitaxially grown onto the SnO_2 carrier accompanied by small RuO_2 nanoparticles, both preferentially exposing {1 1 0} and {0 1 1} crystal facets. This description applies also to the binder-containing catalyst, as the presence of alumina has been shown not to affect the morphology of RuO_2/SnO_2 [19]. DFT analysis of the elementary steps of the reaction mechanism already reported for RuO_2(1 1 0) [14,16] and extended above to different surface facets predicts a higher activity in HCl oxidation for the (1 1 0) and (0 1 1) planes over the (1 0 0) plane. Further, the calculations on mono-/bilayers of RuO_2 on SnO_2 indicate that the supported RuO_2 bilayer is more active than the unsupported RuO_2 (Fig. 4). The latter outcome is tentatively related to a less effective self-poisoning of RuO_2 by chlorine in view of the geometric effect caused by epitaxy, which relates well to the easier chlorine evolution evidenced in the TAP data. The similar transients obtained for equilibrated RuO_2/SnO_2 (Fig. 7a–c) seem to indicate that the main mechanistic features are retained, and in spite of the strong morphological changes, this material underwent upon use, leading to the formation of larger nanoparticles by sintering [19]. Even in this scenario, the gap to bulk RuO_2 is still significant. Regarding the H_2O responses (Fig. 7b), the situation appears reversed in the sense that the response of RuO_2/SnO_2–Al_2O_3 is broader than that of RuO_2, showing a t_{max} higher by 0.4 s and a $t_{h/2}$ shifted to longer times by 0.4 s as well. This difference is not due to experimental artifacts, since the Kr responses are practically identical in all cases, but most likely relates to the presence of alumina in the former sample. Therefore, the TAP response suggests that alumina affects the adsorption/desorption equilibrium of water, inducing a somewhat more impeded evolution of this product from the binder-containing catalyst. As for the RuO_2/SnO_2 catalyst, again, it shows a promoted product desorption with respect to RuO_2 indicating the role of structural effects, upon supporting ruthenium, in the reaction.

Valuable insights into the reaction mechanism on RuO_2/SnO_2–Al_2O_3 were obtained from the examination of the Cl_2 responses in pump–probe experiments. A detailed description of these experiments was given in Refs. [19,26]. These measurements were systematically obtained with O_2 and HCl exchanging their roles (O_2 pump and HCl probe or HCl pump and O_2 probe). The time delay between the pump and probe pulses (Δt) was varied in the range of 1–12 s, which enables to study the influence of the pump molecule coverage on the Cl_2 production. The consecutive cycles were linked in such a way that the time elapsed between the probe pulse and the pump pulse of the next cycle was always 10 s. The coverage of the probe molecule at the beginning of the cycle is therefore very low, since the probe pulse has almost entirely eluted after 10 s. The transient responses of Cl_2 over RuO_2/SnO_2–Al_2O_3 are presented in Fig. 8. Chlorine production progressively decreases as Δt increases both when O_2 is the pump (Fig. 8a) and when HCl is the pump (Fig. 8b). This trend is qualitatively identical to RuO_2 [18] and indicates that the catalytic activity depends on the coverage of both adsorbed species. Further details on the mechanism can be attained by the analysis of the Δt effect on the total Cl_2 production (Fig. 8c). When O_2 is the pump molecule, increasing the time until HCl is pulsed (Δt) from 1 to 12 s provokes a decrease in Cl_2 production of ca. 100%. This is a direct evidence of reaction with adsorbed oxygen. Similarly, when HCl is the pump, an important decrease in Cl_2 production with increasing Δt (ca. 120%) is observed, implying that the reaction occurs through adsorbed Cl species. These data support that HCl oxidation on RuO_2/SnO_2–Al_2O_3 proceeds via a Langmuir–Hinshelwood mechanism, in line with the observations made for bulk RuO_2 and RuO_2/TiO_2 catalysts [18] and also in agreement with PGAA data.

3.7. Micro-kinetic modeling

From the reaction energy profiles shown in Fig. 4 and the corresponding partition functions, we have evaluated several experimental parameters discussed in above sections. In the micro-kinetic (MK) models, a minimum of 12 elementary steps (Eqs. (2)–(7), plus the reverse reactions) and the site balance have been taken into account for each of the studied surfaces (1 1 0), (1 0 1), and (1 0 0). With the MK model, it is possible to self-consistently obtain the populations of intermediates (O_2, O, Cl, OH, H_2O) at the surface and the reactivity as either reaction rate or turnover frequency, TOF_{Cl2} in s^{-1}, at a given time.

As benchmark, we have calculated the TOF for the RuO_2(1 1 0) and (1 0 0) surfaces, at the conditions reported by Over et al. [40] ($p(O_2)$ = 0.5 mbar, p(HCl) = 2 mbar, T = 650 K), considering the conversion after 2 h as in their experiments. The calculated value on RuO_2(1 1 0) using the formula in their work is 0.61 s^{-1}, while the experimental estimate is 0.6 s^{-1}. The agreement found between our MK results and the low-pressure experimental value is, thus, particularly remarkable, and gives a strong support to the validity of the present approach. Low-pressure experiments were also carried out for the (1 0 0) surface. In that case, the experimental estimate is 0.6 s^{-1}, as well that contrasts slightly the calculated TOF value of 1.12 s^{-1}. The origin of this difference might be related to the ability of the (1 0 0) surface to reconstruct into (1 1 0)-like facets. Indeed, a similar reconstruction has been already proposed for TiO_2(1 0 0) [41]. The surface energies for the (1 1 0) and (1 0 0) surfaces are γ_{110} = 0.041 and γ_{100} = 0.047 eV $Å^{-2}$ and the difference can be the driving force for reconstruction. The reconstruction would account then for the similar reactivity of both (1 1 0) and (1 0 0) surfaces observed experimentally. Finally, it is important to notice that the Wulff construction and the XRD pattern of pure RuO_2 powder seem to indicate 10–15% contribution of this (1 0 0) facet, though X-ray diffraction is a bulk technique and thus cannot precisely determine if the topmost layers are partially reconstructed. Therefore, in modeling a nanoparticle structure, we neglected the (1 0 0) facet. Based on the above discussion, in the MK modeling of case "RuO_2 nanoparticle," we have employed a relative surface area for the (1 1 0) facet of about 58% and 42% (1 0 1). As we will see later, these results are robust enough as small modifications in these values do not change the trends observed.

In order to gain further insight into the mechanism, we have investigated the inhibiting role of reaction products. For this, the micro-kinetic model on the nanoparticle structure, MK–NP, was investigated at T = 573 K, $p(O_2)$ = 0.2 bar, and p(HCl) = 0.2 bar with variable initial pressures of either Cl_2 or H_2O in the range of 0–0.6 bar. The results are displayed in Fig. 9. Although the effect shown here for H_2O is smaller than in Fig. 3b, the micro-kinetic model based on the DFT-calculated parameters does tend to qualitative reproduce the flow experiments, and a reduction in the overall activity is obtained when increasing the pressure of the products at the reactor inlet.

We have analyzed in detail the dependence of the reaction rate to the intermediates adsorbed on the surface with the aim of unraveling the origin for the observations in the PGAA experiments. For this purpose, we have simulated the experimental conditions used during PGAA (p(HCl) = 0.2 bar, 573 K) by varying the $p(HCl):p(O_2)$ ratio from 1:4 to 1:0.25, see Fig. 10. To better understand the data, we have proceeded as follows, first the individual (1 1 0) and (1 0 1) surfaces have been analyzed and the rates for these surfaces as a function of the surface coverages obtained. In the second step, a nanoparticle containing both (1 1 0) and (1 0 1) surfaces was considered. Finally, the role of the SnO_2 support was studied in a different set of computational experiments, Fig. 11. To compare all reaction rates in the batch MK model, the production of Cl_2 was obtained always at the same time (t = 0.1 s).

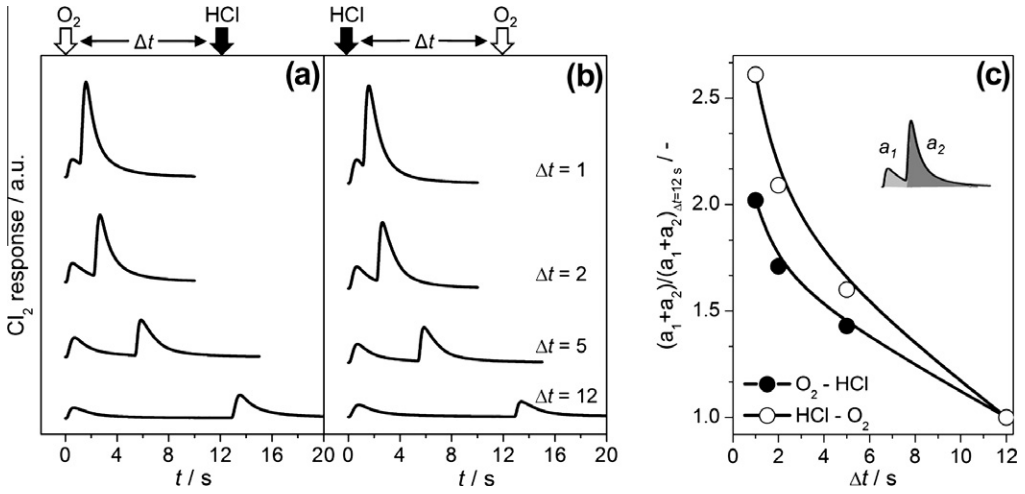

Fig. 8. Transient responses of Cl_2 over RuO_2/SnO_2–Al_2O_3 in pump–probe experiments of (a) O_2 and HCl and (b) HCl and O_2 at different time delays and 623 K. (c) Normalized related to Cl_2 production derived from these experiments. The total Cl_2 production, defined as the sum of the areas in the pump (a_1) and probe (a_2) pulses, was normalized to the experiment at Δt = 12 s.

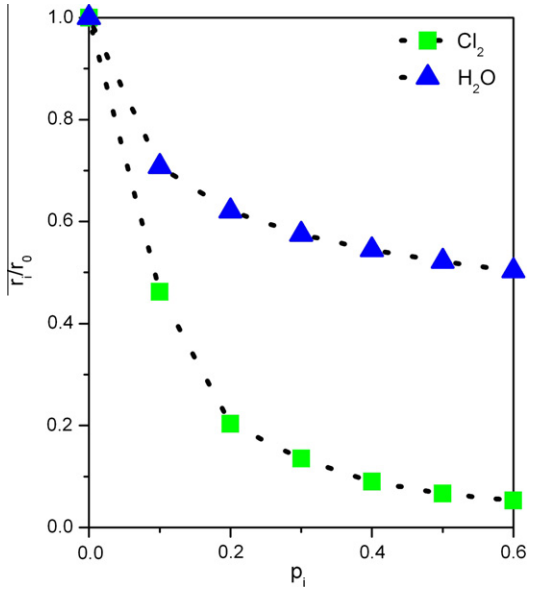

Fig. 9. Micro-Kinetic results: Dependence of the relative rate, r_i/r_0, with the pressures of products at the inlet, p_i of H_2O or Cl_2 (in bar). The r_0 reaction conditions correspond to 0.2 bar for both reactants, HCl and O_2 at 573 K and without any products present at the inlet. All rates determined under initial rate conditions. r and r_0 have the same meaning as in Fig. 3.

Starting by the RuO_2(1 1 0) MK model, the reaction rate is found to be dependent on the chlorine coverage at Ru_{cus} sites, see Fig. 10a. Under the conditions in the experiment, the values of Cl coverage observed are high (though its absolute number is not estimated) and thus Cl is likely the most abundant reactive intermediate. The largest activity is retrieved for the 1:4 p(HCl):p(O_2) ratio and decays along the series when less O_2 is present. The dependence observed shows almost a linear negative slope indicative of the self-poisoning effect of Cl under such conditions. Obviously, the inverse slope is found when the dependence with the coverage of non-chlorine species $1-\theta_{Cl,}$ is investigated. For the (1 0 1) surface, the situation is somewhat different, as the intrinsic activity seems to be lower, and the chlorine coverage is much smaller than for the (1 1 0) facet, about 0.6 ML. Also in this case, the negative slope found for θ_{Cl} results into positive dependence when $1-\theta_{Cl}$ or θ_O are considered (see central panel). Nevertheless, geometric constraints on the (1 0 1) surface seem to give rise impeded activity as the total coverage of all species is always lower than on the (1 1 0) surface due to strong repulsions along the Ru_{cus} chains.

The MK–NP model shows a mixed behavior, the reaction rate is about a half of that of the most active surface (surface fractions are 58% (110) and 42% (101)), and the θ_{Cl} coverage is obviously also much higher than for the (1 0 1) facet, but smaller than that of the (1 1 0) one. The dependence of the activity with the amount of chlorine on the surface is again negative, indicative of the poisoning effect of surface chlorine. As for the individual facets, positive dependencies with the amount of oxygen on the surface or with $1-\theta_{Cl}$ are found. These results suggest that there is an optimum relationship between the Cl and O coverages that provides the most active catalytic phase. More importantly, for highly covered Cl surfaces, the difficulties in finding two neighboring open Ru_{cus} sites can block O_2 dissociative adsorption impeding the re-oxidation and preventing the catalytic process to complete the cycle. Thus, we conclude that though Cl recombination is the elementary step with the highest barrier, at high Cl coverages, the high stability of Cl_{cus} drives O_2 dissociative chemisorption as the likely rate limiting step. Additionally, geometric constrains enhance differences in the reactivity of different facets. Finally, we have determined the apparent activation energy for the NP case by determining the MK-calculated activity at different temperatures. In the region 400–673 K, the obtained estimate is 72 kJ mol^{-1}, in reasonable agreement with the results in the catalytic test section (69 kJ mol^{-1}).

The results for the RuO_2 adlayers on SnO_2(1 1 0) surface have been analyzed with the same methodology, see Fig. 11. The reaction rate obtained for the RuO_2/SnO_2 (1 ML) is close to zero for all HCl:O_2 ratios, showing that this model surface is not active at 573 K, and thus is the least active of all investigated surfaces. Instead, the activity observed for the RuO_2/SnO_2 (2 ML) is slightly higher than that observed for the pure RuO_2(1 1 0) at the same time. Again, the activity depends negatively on the chlorine coverage (θ_{Cl}) of the surface. The corresponding oxygen coverage is even smaller than for the (1 1 0) surface, but in both cases, a positive dependence on the calculated O_{cus} coverage and the total fraction of non-chlorine-containing sites ($1-\theta_{Cl}$) is obtained.

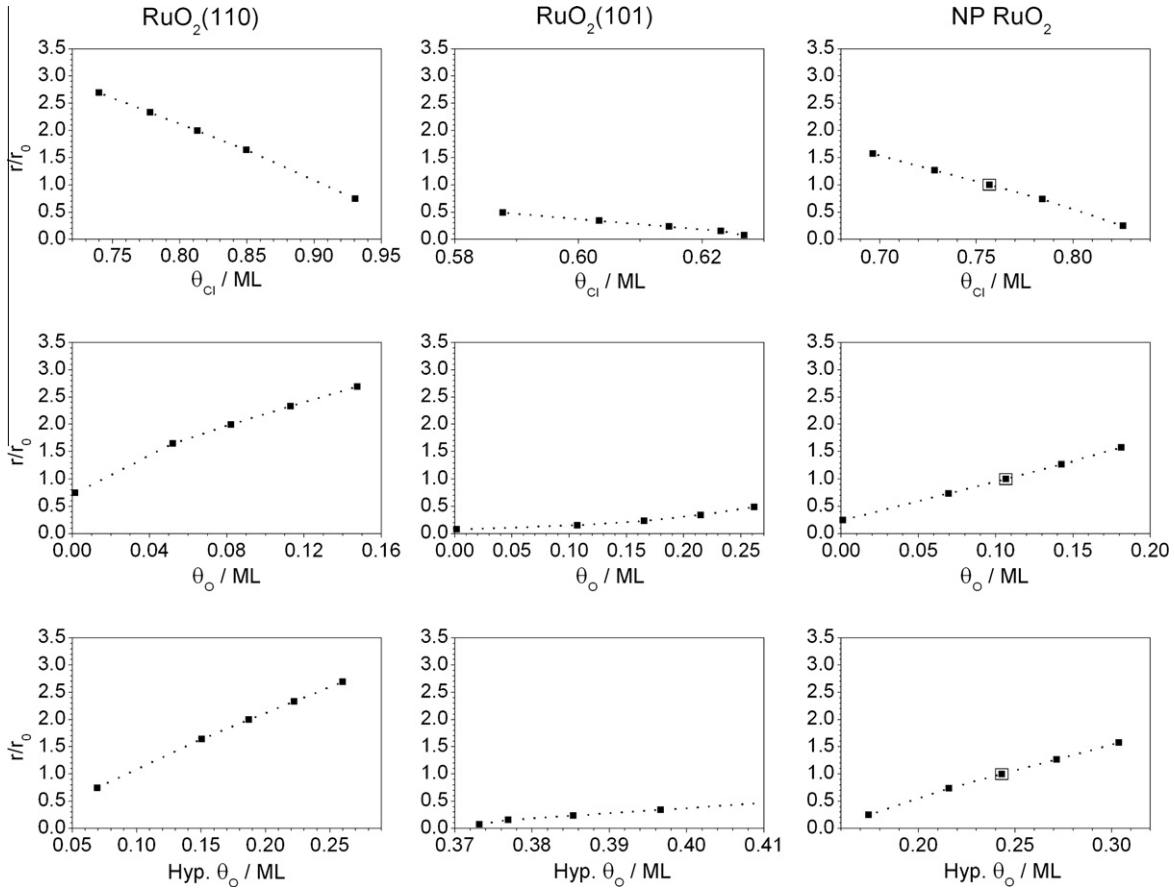

Fig. 10. Micro-Kinetic results: Chlorine, θ_{Cl}, oxygen, θ_O, and $1-\theta_{Cl}$ coverage (in rows) at cus position obtained with the micro-kinetic model at initial pressures of 0.2 bar of HCl and varying p(O_2) pressures (ratios = 1:0.25, 1:0.5, 1:1, 1:2, 1:4) at 573 K and the corresponding normalized reaction rate (r/r_0 at t = 0.1s) for RuO_2(1 1 0), RuO_2(1 0 1), and the nanoparticle, NP (in columns). All data are normalized to the NP case at 1:1 feed ratio.

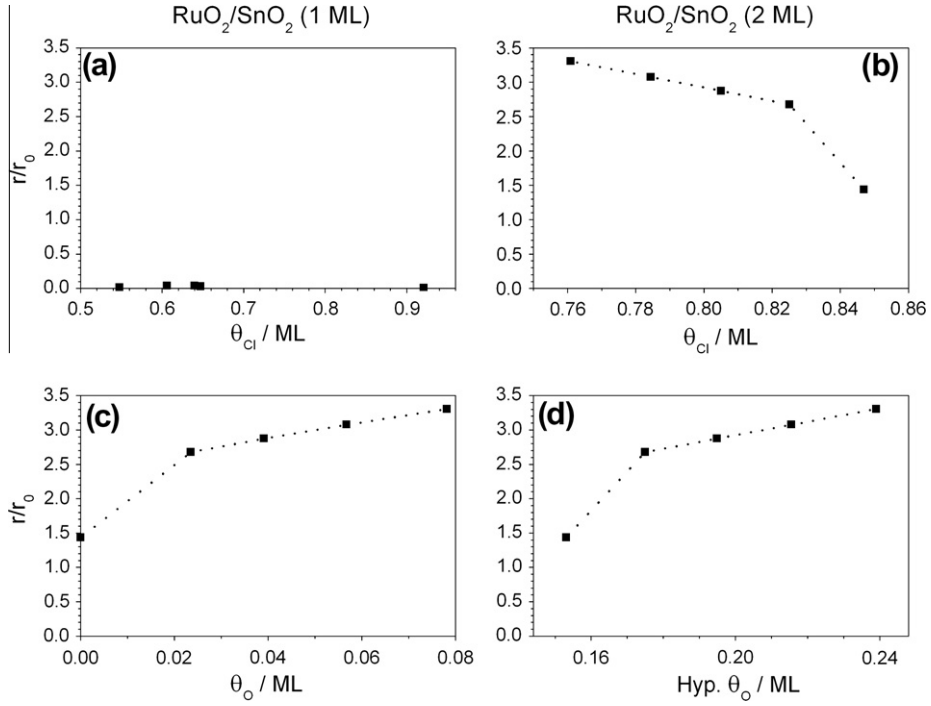

Fig. 11. (a) Micro-Kinetic results: Normalized reaction rate as a function of chlorine cus coverage, θ_{Cl}, for the HCl:O_2 ratios of = 1:0.25, 1:0.5, 1:1, 1:2, 1:4 at 573 K and the single monolayer on the SnO_2(1 1 0) surface RuO_2/SnO_2(1 ML). (b) Same as (a) for the RuO_2 bilayer, RuO_2/SnO_2(2 ML). (c) Normalized reaction rate as a function of the calculated cus oxygen coverage θ_O for the bilayer model RuO_2/SnO_2(2 ML). (d) Same as (c) for the $1-\theta_{Cl}$ coverage. All data are normalized to the NP case at 1:1 feed ratio (Fig. 10).

DFT-based MK modeling was capable to reproduce all trends observed in steady-state catalytic experiments and during PGAA. Deacon reaction over RuO_2 catalysts thus follows the Langmuir–Hinshelwood mechanism with oxygen activation being rate determining under typical Deacon conditions.

4. Conclusions

This article describes experimental and computational results that helped to assess realistic aspects as well as mechanistic details of Deacon reaction over a technical RuO_2-based catalyst. We applied, beyond standard characterization techniques, state-of-the-art experimental methods (aberration-corrected HRTEM, TAP, in situ PGAA) in concert with DFT calculation and micro-kinetic modeling. HRTEM shows that two major RuO_2 morphologies are present in RuO_2/SnO_2 catalysts, namely 2–4-nm-sized particles and 1–3-ML-thick epitaxial RuO_2 films attached to the SnO_2 support particles. A large fraction of nanoparticles exposes {1 1 0} and {1 0 1} type facets. Steady-state kinetic experiments indicate that both reactants display positive rate dependence (HCl: 0.2; O_2: 0.4 order), whereas products cause strong inhibition. When both products are co-fed, the reaction order of HCl and O_2 gets 0.5 and 1, respectively. Pump–probe experiments conducted in the TAP reactor clearly indicated a reaction mechanism within adsorbed species, without the influence of bulk oxygen (Langmuir–Hinshelwood). By using in situ PGAA, we demonstrated that adsorbed Cl poisons the surface and the reactivity is proportional to the coverage of a "non-Cl," likely adsorbed oxygen species. All experimental observations (kinetic trends, coverage effects) were conciliated with DFT-based micro-kinetic modeling. Calculations additionally indicated that the reaction, despite previous claims, is structure sensitive. The (1 0 0) and (1 1 0) facets, as well as the 2 ML RuO_2 film-covered SnO_2 give rise to significantly higher reactivity as compared to the (1 0 1) surface, whereas the 1 ML RuO_2 film seems to be inactive. At typical reaction conditions, the surface is extensively chlorinated; thus, the active material is better described as a surface oxy-chloride. Despite the highest barrier of Cl recombination, under realistic Deacon conditions, oxygen activation is rate determining.

Acknowledgments

We thank Bayer MaterialScience AG for permission to publish these results. Drs. M.A.G. Hevia and L. Durán-Pachón (ICIQ Tarragona) are acknowledged for experimental input. ETH Zurich, the BMBF Project 033R018A, and MICINN (CTQ2009-07753/BQU, CSD2006-0003) are thanked for financial support and BSC-RES for providing generous computational resources. For the in situ PGAA measurements, we acknowledge the financial support of the EU FP7 NMI3 Access Programme and the NKTH NAP VENEUS Grant (OMFB-00184/2006).

Appendix A. Supplementary material

Supplementary data associated with this article can be found, in the online version, at doi:10.1016/j.jcat.2011.09.039.

References

[1] www.eurochlor.org.
[2] A.J. Johnson, A.J. Cherniavsky, US Patent 2542,961, 1951.
[3] F. Wattimena, W.M.H. Sachtler, Stud. Surf. Sci. Catal. 7 (1981) 816.
[4] T. Kiyoura, N. Fujimoto, M. Ajioka, T. Suzuki, Y. Kogure, K. Kanaya, T. Nagayama, EP184413-A, 1984.
[5] T. Hibi, H. Nishida, H. Abekawa, US Patent 5871,707, 1999.
[6] T. Hibi, H. Abekawa, K. Seki, T. Suzuki, T. Suzuta, K. Iwanaga, T. Oizumi, EP936184, 1999.
[7] T. Hibi, T. Okuhara, K. Seki, H Abekawa, H. Hamamatsu, WO200110550-A1, 2001.
[8] K. Iwanaga, K. Seki, T. Hibi, K. Issoh, T. Suzuta, M. Nakada, Y. Mori, T. Abe, Sumitomo Kagaku (2004).
[9] K. Seki, Catal. Surv. Asia 14 (2010) 168.
[10] A. Wolf, L. Mleczko, O.F. Schlüter, S. Schubert, EP2026905, 2006.
[11] A. Wolf, J. Kintrup, O.F. Schlüter, L. Mleczko, EP2027062, 2006.
[12] A. Wolf, L. Mleczko, S. Schubert, O.F. Schlüter, EP2027063, 2006.
[13] J. Heemskerk, J.C.M. Stuiver, DE1567788, 1964.
[14] S. Zweidinger, D. Crihan, M. Knapp, J.P. Hofmann, A.P. Seitsonen, C.J. Weststrate, E. Lundgren, J.N. Andersen, H. Over, J. Phys. Chem. C 112 (2008) 9966.
[15] D. Crihan, M. Knapp, S. Zweidinger, E. Lundgren, C.J. Weststrate, J.N. Andersen, A.P. Seitsonen, H. Over, Angew. Chem. 120 (2008) 2161.
[16] N. López, J. Gómez-Segura, R.P. Marín, J. Pérez-Ramírez, J. Catal. 255 (2008) 29.
[17] F. Studt, F. Abild-Pedersen, H.A. Hansen, I.C. Man, J. Rossmeisl, T. Bligaard, ChemCatChem 2 (2010) 1.
[18] M.A.G. Hevia, A.P. Amrute, T. Schmidt, J. Pérez-Ramírez, J. Catal. 276 (2010) 141.
[19] C. Mondelli, A.P. Amrute, F. Krumeich, T. Schmidt, J. Pérez-Ramírez, ChemCatChem 3 (2011) 657.
[20] Z. Revay, T. Belgya, L. Szentmiklosi, Z. Kis, A. Wootsch, D. Teschner, M. Swoboda, R. Schlogl, J. Borsodi, R. Zepernick, Anal. Chem. 80 (2008) 6066.
[21] D. Teschner, J. Borsodi, A. Wootsch, Z. Revay, M. Havecker, A. Knop-Gericke, S.D. Jackson, R. Schlogl, Science 320 (2008) 86.
[22] Z. Revay, Anal. Chem. 81 (2009) 6851.
[23] J.T. Gleaves, G.S. Yablonsky, P. Phanawadee, Y. Schuurman, Appl. Catal. A 160 (1997) 55.
[24] J. Pérez-Ramírez, E.V. Kondratenko, Catal. Today 121 (2007) 160.
[25] A.P. Amrute, C. Mondelli, M.A.G. Hevia, J. Pérez-Ramírez, J. Phys. Chem. C 115 (2011) 1056.
[26] A.P. Amrute, C. Mondelli, M.A.G. Hevia, J. Pérez-Ramírez, ACS Catal. 1 (2011) 583.
[27] G. Kresse, J. Hafner, Phys. Rev. B 47 (1993) 558.
[28] G. Kresse, J.M. Furthmüller, Phys. Rev. B 54 (1996) 11169.
[29] B. Hammer, L.B. Hansen, J.K. Nørskov, Phys. Rev. B 59 (1999) 7413.
[30] G. Kresse, D. Joubert, Phys. Rev. B 59 (1999) 1758.
[31] G. Wulff, Z. Krystallogr. Min. 34 (1901) 449.
[32] I. Chorkendorff, J.W. Niemantsverdriet, Concepts of Modern Catalysis and Kinetics, Wiley–VCH, Weinheim, 2003.
[33] G. Novell-Leruth, J.M. Ricart, J. Pérez-Ramírez, J. Phys. Chem. C 112 (2008) 13554.
[34] http://www.maplesoft.com/products/maple/.
[35] N. Lu, Q. Wan, J. Zhu, J. Phys. Chem. Lett. 1 (2010) 1468.
[36] M. Batzill, K. Katsiev, J.M. Burst, U. Diebold, A.M. Chaka, B. Delley, Phys. Rev. B 72 (2005) 165414.
[37] http://webbook.nist.gov/chemistry (retrieved December 2010).
[38] H. Wang, W.F. Schneider, D. Schmidt, J. Phys. Chem. C 113 (2009) 15266.
[39] D. Teschner, et al., Unpublished results.
[40] S. Zweidinger, J.P. Hofmann, O. Balmes, E. Lundgren, H. Over, J. Catal. 272 (2010) 169.
[41] P.D.J. Lindan, N.M. Harrison, Surf. Sci. 479 (2001). L375.